Nanoscale

PAPER

Cite this: *Nanoscale*, 2017, **9**, 14395

Efficient photoelectrochemical water splitting on ultrasmall defect-rich TaO_x nanoclusters enhanced by size-selected Pt nanocluster promoters†

Saurabh Srivastava, Joseph Palathinkal Thomas, Nina Heinig, Marwa Abd-Ellah, Md Anisur Rahman and Kam Tong Leung *

Formation of nanoclusters has attracted a lot of attention in recent years because of their distinct properties from isolated atoms and bulk solids. Here, we focus on the catalytic properties of supported transition metal oxide nanoclusters, such as TaO_2, with a well-defined size distribution below 10 nm. We show that their catalytic performance can be greatly enhanced by introducing a reaction promoter such as Pt. Different combinations of precisely size-selected, defect-rich TaO_x and Pt nanoclusters are produced by a gas-phase aggregation technique in a special DC magnetron sputtering system. Argon flow rate and aggregation length are carefully optimized to control the sizes of these ultrasmall TaO_x and Pt nanoclusters by using a quadrupole mass filter, and TEM studies reveal the different crystalline nature of TaO_x (amorphous) and Pt (crystalline) nanoclusters. We have further demonstrated the size-dependent photoanode activity of (TaO_x, Pt) nanocluster systems in a photoelectrochemical water splitting reaction, where the Pt nanocluster promoters are found to provide a significant enhancement in the photocurrent density, approximately tripled that was observed from just TaO_x nanocluster catalysts alone. The photocurrent density and photoconversion efficiency tend to reduce when Pt nanoclusters become overpopulated due to blocking of the photosensitive TaO_x surface. Reducing the Pt nanocluster size resolves this problem by incorporating a greater number of smaller nanocluster promoters without blocking TaO_x, which leads to further enhancement in the photocurrent density. The enhanced photocatalytic activity is attributed to synergetic effects introduced by the Pt nanoclusters that act as temporary charge storage sites to facilitate effective separation of a large number of electron–hole pairs, generated from a large number of active sites on the defect-rich amorphous TaO_x nanoclusters upon illumination.

Received 18th June 2017,
Accepted 22nd July 2017

DOI: 10.1039/c7nr04378c

rsc.li/nanoscale

Introduction

Nanoscience generally focusses on the study of the generation and structure–property relationship of nanosized materials.[1] The term "nanoclusters" is used to describe aggregates of atoms and molecules with characteristic dimensions of a few nanometers.[2] Nanoclusters (NCs) provide a direct link between the distinct behavior of isolated atoms and molecules on the one hand and their bulk counterparts on the other hand. As NCs have a much larger surface area to volume ratio (specific surface area) than bulk matter, they provide an excellent testing ground to study surface-related properties, particularly surface reactivity. In the past decade, NCs of transition metal oxides have been used in numerous applications in catalysis, sensors, optoelectronic and magnetic devices.[3–9] These applications all require the creation of stable assemblies or arrays of nanoclusters that could maintain their properties (without degradation over time) with respect to the relevant operating environment. While most of the transition metals and their oxides have exhibited these properties separately on their own, a combination of two or more types of NCs on a single substrate could lead to cooperative, parallel or sequential catalytic processes, which would open up new opportunities for novel cluster applications. With the development of nanocluster molecular beam systems, which have been providing fundamental understanding of gas-phase reaction dynamics and catalysts of "free" NCs for several decades,[10,11] there has been a recent surge in interest in producing uniformly distributed, discrete size-selected NCs onto different substrates (*i.e.*, the "supported" NCs) and the applications of these supported NCs.[12–15] Among the various techniques used for depositing

WATLab and Department of Chemistry, University of Waterloo, Waterloo, Ontario, N2L3G1, Canada. E-mail: tong@uwaterloo.ca

†Electronic supplementary information (ESI) available: Photocurrent densities for different Pt nanocluster sizes, highly stable photocurrent density over a long time, photocurrent densities under UV and Visible light illumination. See DOI: 10.1039/c7nr04378c

transition metal NCs onto surfaces, the gas-phase aggregation technique has shown the most promise in the synthesis of free and supported NCs.[16–18] To date, there have been a number of studies focused on the NCs of transition metals (Cu,[18] Ag,[19] Au,[20] and Pd[21]), metal alloys (Au/Pd[22] and Cu/Au[23]) and metal oxides (TiO_2 [24–26] and ZnO[27]) generated by the gas-phase aggregation technique.

Recently, Ta_2O_5 has become an important new material for various emerging applications because of its higher chemical stability compared to other transition metal oxides (*e.g.* TiO_2, Fe_2O_3, and CuO) and its high dielectric constant.[28] The redox potentials of H^+/H_2 (0 V *vs.* RHE) and O_2/H_2O (+1.23 V *vs.* RHE) are well within the conduction band minimum and valence band maximum of Ta_2O_5, which makes Ta_2O_5 a promising high-performance catalyst material for solar water splitting. Furthermore, Ta_2O_5 rich with surface and bulk oxygen vacancy defects (often termed TaO_x, $1 < x < 2.5$) offers potential enhancement in the photocatalytic performance particularly in the visible light region. An assembly of discrete TaO_x NCs would therefore be of great interest not only because of their high specific surface area, which provides a large number of reaction sites (per volume), but also due to their modified electronic structures with appropriate energy band separations for electron–hole pair generation for photoelectrochemical water splitting reaction triggered by visible solar light. However, one potential limit on the performance is the high recombination rate of photogenerated electron–hole pairs. Instead of relatively complex structural modification in Ta_2O_5 nanostructures,[29] such as by using NiO[30] or SiO_2 as co-catalysts, and by doping with nitrogen (*e.g.* TaON and Ta_2N_3)[31] or even by creating tantalates,[32] we present here a (TaO_x, Pt) composite nanocluster system in order to alleviate the high recombination rate problem and increase the solar energy harvesting of semiconductor-based photocatalysts by using Pt as a reaction promoter. With the advantage of their plasmonic properties, metallic NCs (Pt in our case) support collective electron oscillation, and the presence of these surface plasmons also helps to concentrate and scatter the light near the semiconductor/liquid interface, potentially leading to more effective light trapping inside the semiconductor and therefore better solar light harvesting. In the present work, we focus on size-selected ultrasmall TaO_x (~5 nm in dia.) and Pt nanoclusters (2.5, 3.5, or 5 nm), created and co-deposited using a gas-phase aggregation technique that is coupled with a built-in quadrupole mass filter for precise size selection [with atomic weights of Ta (Z = 73): 180.945 amu, and Pt (Z = 78): 195.078 amu]. Co-deposition (by sputtering individual targets simultaneously or sequentially) can be used to create a well-mixed population of both nanoclusters, in order to achieve effective electron–hole pair separation. While Ta and Pt have the propensity to form intermetallic alloy phases during sputtering at an elevated temperature,[33,34] deposition at room temperature (employed here) would produce a nearly pure phase for both NCs (with an undetectably low degree of intermixing at room temperature). As monosized NCs on substrates have the tendency to agglomerate on the surface, we resolve this difficulty by ensuring low-energy, soft-landing of NCs onto the substrates. We further demonstrate the excellent photoelectrochemical catalytic performance of the (TaO_x, Pt) NC composite film deposited on silicon substrates. As a high density of defects is inherently beneficial for potential applications in surface-dependent catalysis and nanoelectronics, the synthesis of a stable, precisely size-selected (TaO_x, Pt) NC composite film with desirable synergetic physicochemical properties promises other emerging applications in photoelectrochemical water splitting, nanoelectronics and other solar-driven technologies.

Experimental

Size-selected NCs of TaO_x and co-deposited (TaO_x, Pt) composites have been produced by using a novel nanocluster generation system (Nanogen, Mantis Deposition Ltd). A DC magnetron sputtering process coupled with gas-phase aggregation, based on the Haberland[35,36] concept of cluster formation, is used to deposit the source materials from the metallic Ta and Pt sputtering targets (99.95% purity, ACI Alloys). A plasma containing Ta and Pt atoms and their ions is generated upon magnetron sputtering in Ar (at 25 W), and the sputtered atoms coalesce into clusters under high pressure collision-prone conditions. Details of the cluster growth mechanism have been given in our previous work.[15] Briefly, source atoms and ions are generated by magnetron sputtering and they then undergo collisional condensation that leads to nucleation and gas-phase aggregation and finally to cluster formation.[36] Based on their mass-to-charge ratio, precise mass selection of NCs with a particular size is achieved by using a quadrupole mass filter with 2% mass resolution before landing onto the substrate. H-Terminated Si(100) (H-Si) substrates are used for the present work. Prior to nanocluster deposition, all the substrates are cleaned ultrasonically in acetone and isopropanol, and also dipped in 2% HF for 10 minutes to remove the native oxide layer and to produce H-termination on the Si substrate. Ta NCs could undergo partial oxidation to TaO_x during deposition, and the exteriors of these TaO_x NCs further oxidize completely (to Ta_2O_5) under ambient conditions (after the sample is removed from the deposition chamber). Pt NCs, on the other hand, remain metallic and stable in air.

The surface morphology, size and crystalline structure of the NCs are characterized by atomic force microscopy (AFM) operated in tapping mode in a Digital Instruments Dimension 3100 Nanoman Nanoscope IV microscope, field-emission scanning electron microscopy (SEM) in a Zeiss Merlin microscope, and transmission electron microscopy (TEM) in a Zeiss Libra 200 MC microscope, respectively. TEM samples are prepared by directly depositing small amounts of both NCs onto a lacey carbon coated copper TEM grid to analyze the crystallinity of NCs individually. The chemical-state composition is analyzed by X-ray photoelectron spectroscopy (XPS) in a Thermo-VG Scientific ESCALab 250 Microprobe, equipped with a monochromatic Al Kα X-ray source (1486.6 eV). The XPS data are

fitted by using the CasaXPS software with a Shirley background. The photoelectrochemical water splitting measurements are performed in a three-electrode system in a quartz cell, where the nanocluster film supported on H-Si is used as the photoanode, and Ag/AgCl (3 M KCl) and Pt are used as the reference and counter electrodes, respectively. The experiments are carried out in an electrolyte solution of 1 M KOH (Sigma Aldrich), prepared in filtered, high-resistivity water (resistivity 18 MΩ cm) at room temperature. The photocurrents are measured using linear sweep voltammetry with a CH Instruments 660A electrochemical workstation, both in the dark and under illumination of a 300 W xenon lamp (300–1000 nm, Oriel Instruments 6258) coupled with an AM 1.5 G filter that delivers simulated sunlight with a power density of 50 mW cm^{-2}.

Results and discussion

Size-selected TaO_x and Pt NCs with specific mass-to-charge ratios have been synthesized by using the nanocluster generation source, shown schematically in Fig. 1a. The average cluster size (diameter) of Ta NCs as a function of Ar flow rate (15–50 sccm) and aggregation length (AL, 10–90 mm) are

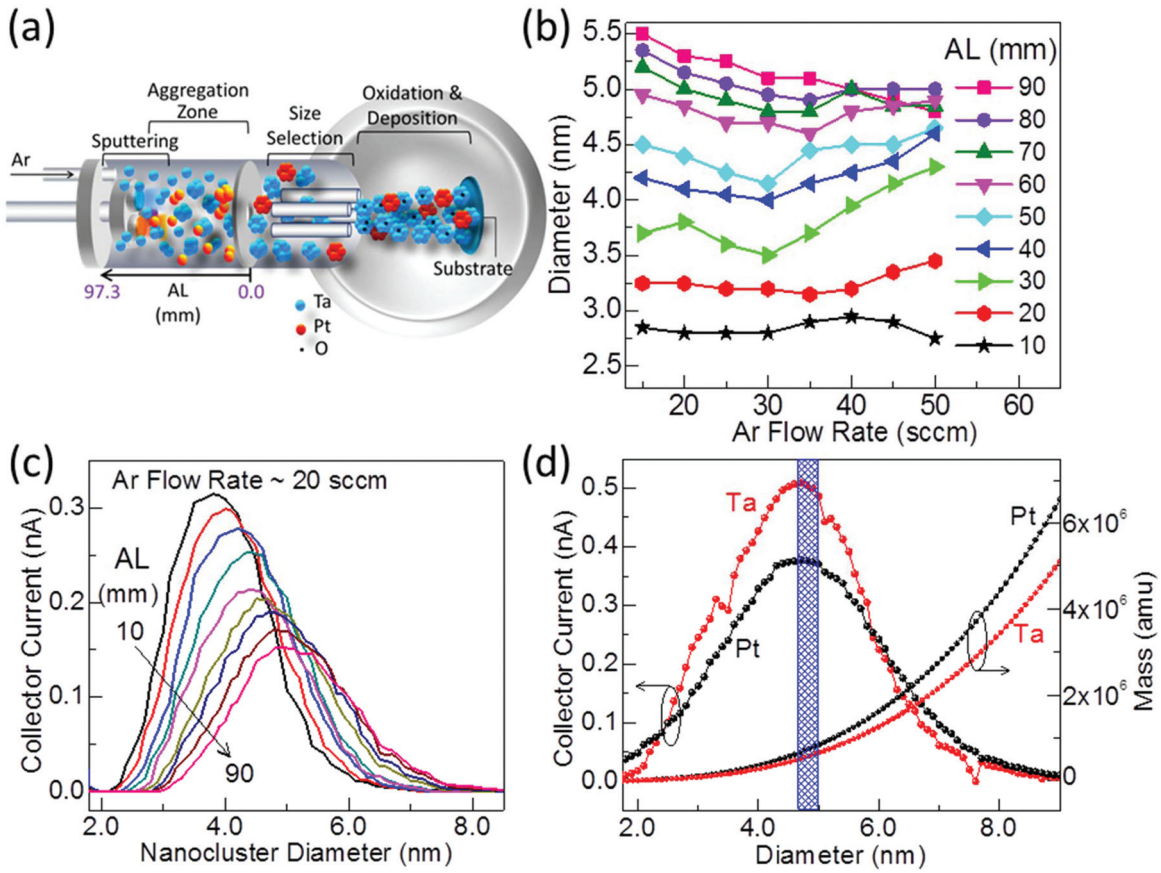

Fig. 1 (a) Schematic diagram of the nanocluster generation source coupled with a quadrupole mass filter for precise size selection (not drawn to scale). Two sputtering targets can be ignited simultaneously to create a composite plasma consisting of two materials (Ta and Pt in this work) through magnetron sputtering. The constituent atoms combine together in the aggregation zone to form Ta_m and Pt_n clusters (*m*, *n* integers), which are transported out of the aggregation zone through a 3 mm dia. orifice by the Ar gas flow. As a large fraction of the clusters are negatively charged, a quadrupole mass filter can be used to perform size selection of the nanoclusters (after exiting through the orifice) based on their mass-to-charge ratio. The size-selected Ta nanoclusters then enter into the main chamber where they become partially oxidized and neutralized to form TaO_x, and deposit onto the substrate under soft-landing conditions. For the size-selected Pt clusters, neutralization (without oxidation) occurs. The aggregation length (AL) corresponds to the distance between the sputtering target and the 3 mm orifice, which can be varied to obtain different nanocluster sizes. (b) Cluster size of Ta (in diameter) as a function of Ar flow rate for different aggregation lengths from 10 to 90 mm (in step of 10 mm). (c) Size distribution as represented by the quadrupole collector current as a function of Ta nanocluster diameter for a fixed Ar flow rate of 20 sccm and variable aggregation lengths from 10 to 90 mm (in step of 10 mm). The mode cluster size is defined as the size for the peak maximum of each distribution curve. (d) Near-Gaussian nanocluster size distribution profiles for the Ta and Pt nanoclusters are measured separately at (40 sccm, 60 mm) with the mode size of 4.7 nm each, where the quadrupole collector current (left axis) is proportional to the cluster population of the specific cluster size. The masses of the nanoclusters (right axis) are also shown as functions of their diameters. The vertical shaded area corresponds to the segment of the cluster size distribution within 2% mass resolution as selected by applying an appropriate set of AC and DC voltages on the quadrupole mass filter.

shown in Fig. 1b. Evidently, the longer the aggregation length in the gas-condensation zone, the larger the NC size. Depending on the aggregation length, the average size of the resulting NCs could decrease (for AL = 90 mm), decrease and then increase (for AL = 20–80 mm), or remain effectively unchanged (for AL = 10 mm) with increasing Ar flow rate, which confirms that both the Ar flow rate and the aggregation length affect the growth kinetics. Argon flow could affect the NC growth not just by initiating the plasma that sputters the source to remove the source atoms from the aggregation zone, but also by providing nucleation seeds for NC growth and serving as a carrier gas for transporting the as-grown NCs towards the substrate. Fig. 1c shows the size distributions as represented by the collector currents as functions of NC size (in diameter) for Ta NCs. The collector current peak maximum is found to decrease with increasing aggregation length, while its peak width (corresponding to the size distribution) increases. After size selection, the broad NC size distribution (Fig. 1c) can be typically restricted to 2% of the full width of the distribution (*i.e.* the mass resolution, Fig. 1d) by applying an appropriate set of AC and DC voltages to the quadrupole mass filter. Further details about parameter optimization and size selection have been discussed elsewhere.[15,37]

Nanocluster deposition is started by igniting the plasma to sputter both Ta and Pt targets simultaneously and then collecting the resulting NCs onto the substrate. The sizes of the Ta NCs are kept fixed at 5 nm whereas the Pt NC sizes are varied from 2.5 nm to 5 nm using an appropriate setting of the quadrupole mass filter (when the Ta and Pt NCs are deposited sequentially). Fig. 1d compares the near-Gaussian size distribution profiles of Ta and Pt NCs (~5 nm each) obtained separately for the same (Ar flow rate, AL) conditions (40 sccm, 60 mm). For other sizes of Pt NCs, (Ar flow rate, AL) conditions are chosen accordingly. The vertical shaded region in Fig. 1d corresponds to parts of nanocluster distributions that are mass-selected within 2% of the respective mode cluster sizes. The respective mass profiles (right axis) as a function of nanocluster size for Ta and Pt NCs produced by the Nanogen cluster source are also shown in Fig. 1d.

Fig. 2a shows the SEM image of TaO_x co-deposited with Pt NCs (5 nm each), with respective total deposition times of 30 min and 15 min (with the corresponding SEM image for TaO_x NCs without co-deposition shown in the inset), on the H-Si substrate. We then increase the Pt total deposition time to 30 min (Fig. 2b) and 45 min (Fig. 2c) while keeping the Ta deposition time fixed at 30 min for the other (TaO_x, Pt) co-depositions. The near-Gaussian size distribution with a mode

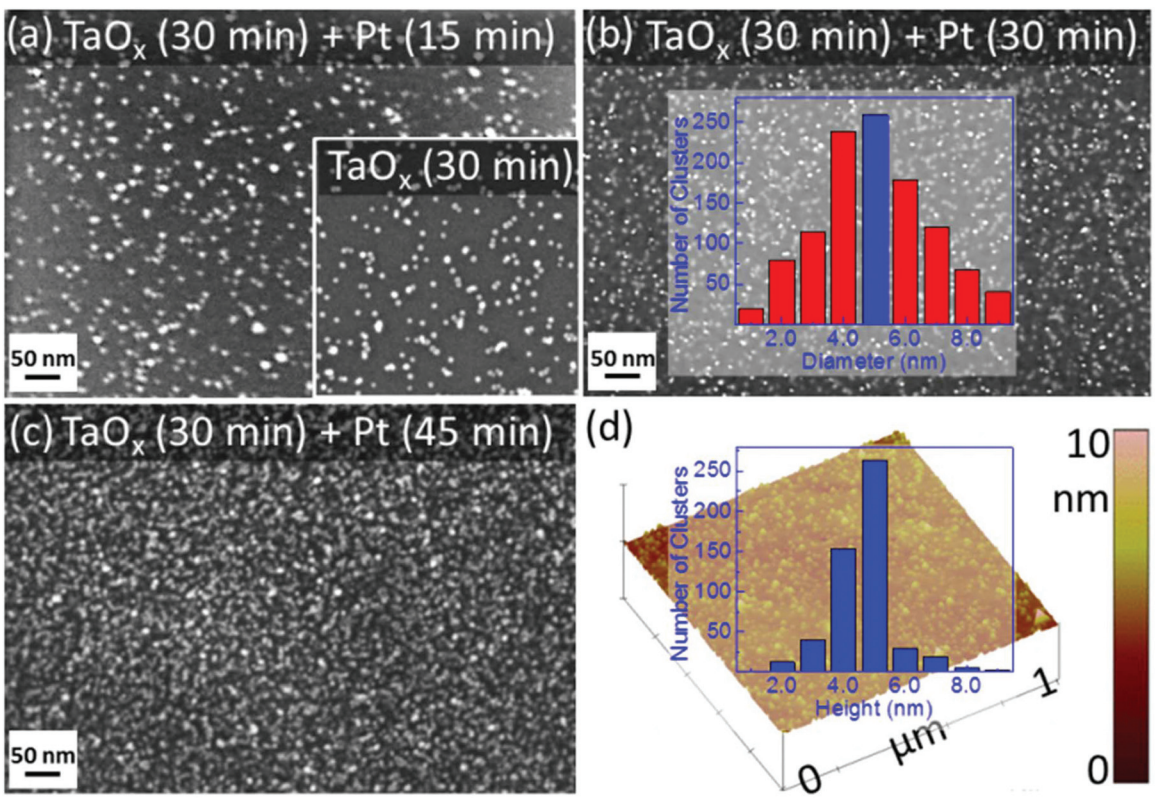

Fig. 2 SEM secondary electron images of TaO_x deposited with deposition parameters (30 sccm, 60 mm) for total Ta deposition time of 30 min without [inset of (a)] and with co-deposition of Pt nanoclusters for (a) 15 min, (b) 30 min and (c) 45 min. The inset of (b) shows the corresponding size distribution before size selection, while the blue area (the highest bar) marks the portion of the nanocluster size-selected by using the quadrupole mass filter. (d) Corresponding AFM image for the sample shown in (b) used to estimate the nanocluster size distribution by using the heights of the nanoclusters, along with the height distribution of the as-deposited (TaO_x, Pt) nanocluster composite (inset).

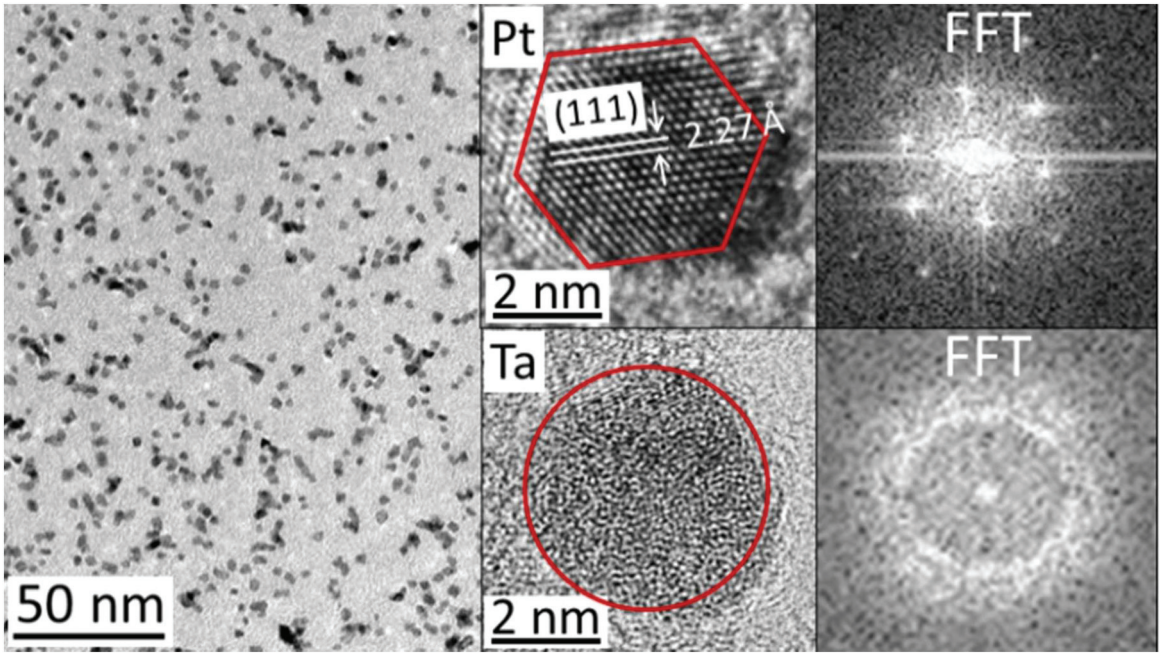

Fig. 3 (Left) TEM image of the (TaO_x, Pt) nanoclusters directly co-deposited for 5 min on a lacey carbon coated copper TEM grid. (Centre) High-resolution TEM images of a Pt and a TaO_x nanoclusters, each of 5 nm dia., depicting a Pt nanocluster with the (111) interplanar spacing of 2.3 Å and an amorphous TaO_x nanocluster. (Right) The corresponding simulated diffraction patterns, as generated by FFT, for the Pt and TaO_x nanoclusters.

size of 5 nm is illustrated for the Ta (30 min) and Pt (30 min) co-deposition in Fig. 2b, inset. Fig. 2d shows the corresponding tapping-mode AFM image of the (TaO_x, Pt) NCs co-deposited for 30 min on a H-Si substrate (with the much narrower size distribution obtained after quadrupole mass filtering as shown in the inset). With the spatial resolution of AFM generally larger than 10 nm, the size of the as-deposited NCs can be estimated from their respective height profile, assuming a spherical shape for the NCs. The size distributions obtained from our *ex situ* SEM and AFM measurements for the as-deposited NCs are therefore found to be in good accord with the collector current profiles of the quadrupole mass filter (Fig. 1d).

The TEM image of the size-selected (TaO_x, Pt) NCs, deposited both for 5 min directly on a TEM grid, shown in Fig. 3 demonstrates the excellent size uniformity of the nanoclusters (~5 nm each) produced by the Nanogen source. High-resolution TEM images of typical nanoclusters reveal the crystalline nature of the Pt NCs (top inset) and the amorphous nature of the TaO_x NCs (bottom inset). The amorphicity of the semiconducting TaO_x NCs gives rise to a higher density of defects, which work as trapping and recombination centers for the photogenerated electron–hole pairs in the photoelectrochemical water splitting process as discussed below. The interplanar spacing of the (111) planes in the Pt NC as determined from the high-resolution image is 2.3 Å, which is in good accord with the Pt FCC crystal structure.[38] The corresponding simulated diffraction patterns obtained by performing FFT on the high-resolution TEM images in Fig. 3 (right column) confirm the specific (111) plane orientation for the crystalline Pt NC and the characteristic ring pattern of the amorphous TaO_x NC. Evidently, there is no detectable alloy formation between TaO_x and Pt NCs, indicating that the Pt and Ta sputtering sources are sufficiently far from each other and there is little interaction between the NCs as-formed in the gas phase.

Fig. 4 shows the depth-profiling XPS spectra of the O 1s, Pt 4f and Ta 4f regions of a typical (TaO_x, Pt) NC film co-deposited with a common mode size of 5 nm on the H-Si (Fig. 2b). For the as-deposited film, the O 1s spectrum (Fig. 4a) exhibits an intense SiO_2 peak at 532.8 eV, with a rather weak shoulder at 530.8 eV consistent with the assignment to Ta_2O_5.[39] Upon sputtering, the maximum of the strong O 1s feature appears to shift to a lower binding energy as the peak becomes broader and less intense, which indicates the emergence of the other oxygen-deficient TaO_x ($1 < x < 2.5$) phase at a lower binding energy. The prominent Pt $4f_{7/2}$ ($4f_{5/2}$) peak at 71.2 (74.5) eV shown in Fig. 4b is attributed to metallic Pt. After 15 s of Ar sputtering, a weak $4f_{7/2}$ ($4f_{5/2}$) peak appears at 72.6 (75.9) eV, and it becomes more prominent upon further sputtering. This feature can be assigned to Pt silicide, Pt_2Si, located at the interface between the Pt NCs and Si. The prominent Ta $4f_{7/2}$ ($4f_{5/2}$) peak at 26.9 (28.8) eV corresponds to Ta_2O_5 (Fig. 4c), in good accord with an earlier report.[31] The presence of the strong Ta_2O_5 feature confirms that the as-grown Ta NCs have been completely oxidized at least in the near-surface region of the NCs. The minor shift in the spectrum towards the lower binding energy is due to the removal of surface hydrocarbons commonly present as a result of ambient handling. A well-defined Ta $4f_{7/2}$ ($4f_{5/2}$) peak is found to emerge at 22.6 (24.5) eV after 30 s of sputtering, and it can be attributed

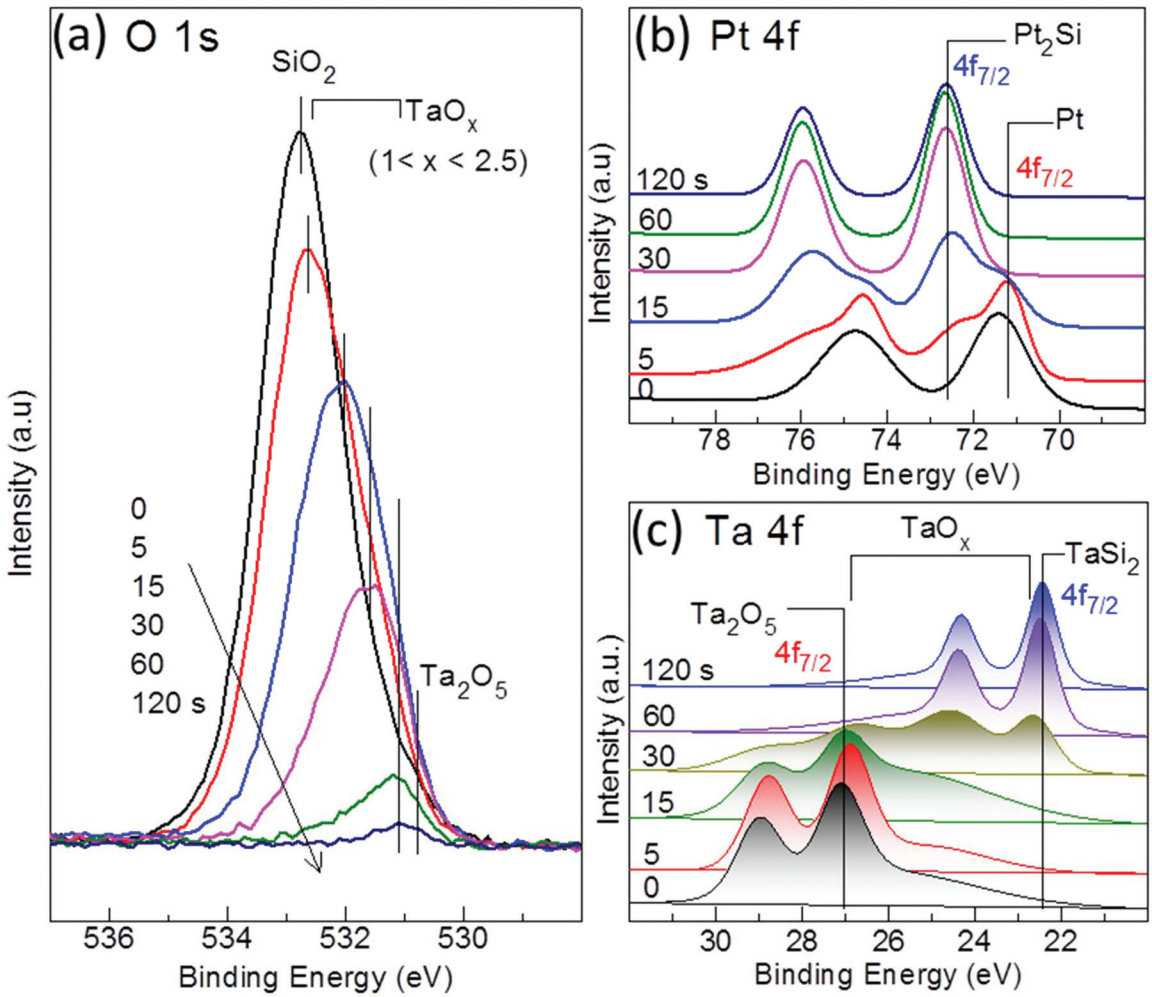

Fig. 4 XPS spectra of (a) O 1s, (b) Pt 4f, and (c) Ta 4f regions for the (TaO_x, Pt) nanoclusters co-deposited for 30 min on a H-Si substrate as a function of Ar sputtering time.

to the TaO_x phase ($1 < x < 2.5$). Upon further sputtering to 60 s, the Ta $4f_{7/2}$ ($4f_{5/2}$) peak at 22.4 (24.4) eV becomes sharper and more intense, which corresponds to the emergence of the $TaSi_2$ phase.[40] Considering the small electron escape depth of ~4 nm,[41] the absence of a metallic Ta peak [expected at 21.8 eV (23.7 eV)][40] before and after a short Ar-sputtering in the XPS spectra for TaO_x confirms the complete oxidation of the nanoclusters.

The photoelectrochemical water splitting properties of the co-deposited (TaO_x, Pt) NC samples are studied under simulated sunlight (with an AM 1.5 G filter) using a three-electrode system connected to an electrochemical workstation. Three (TaO_x, Pt) NC films co-deposited on H-Si substrates with a fixed TaO_x NC amount and three different Pt NC loading amounts (as shown in Fig. 2), each with a mode size of ~5 nm for both TaO_x and Pt NCs, are used as photoanodes. All the photocurrent measurements are conducted for an illumination area of 5×5 mm^2 with a power density of 50 mW cm^{-2} (half a sun), in accordance with our previous work.[15] Before discussing the photocatalytic reactions of the NCs, it is important to emphasize that the bare H-Si substrate shows no photoresponse in the dark or upon illumination with the simulated sunlight (data not shown). Fig. 5a and b show the schematic diagrams for the transfer and separation of photogenerated electrons and holes on the TaO_x NC semiconductor surface, respectively, in the absence and presence of metallic Pt NCs. The presence of Pt NCs in the system as plasmonic particles promotes the water splitting reaction by efficiently concentrating and scattering the intense light near the semiconductor surface.[42,43] In effect, it increases the number of photogenerated carriers that can reach the semiconductor/electrolyte interface and participate in the desired photoelectrochemical water splitting reaction to produce O_2 and H_2. With the absence of Pt NCs (Fig. 5a), the actual amounts of separated electrons and holes are less because of their fast recombination and therefore the photocatalytic activity becomes limited. In contrast, with the presence of Pt NCs (Fig. 5b), the electron–hole pairs are separated efficiently with the transfer of electrons to the nearby Pt NC surface (with more and more Pt NCs in closer contact with the TaO_x NCs with increasing number of

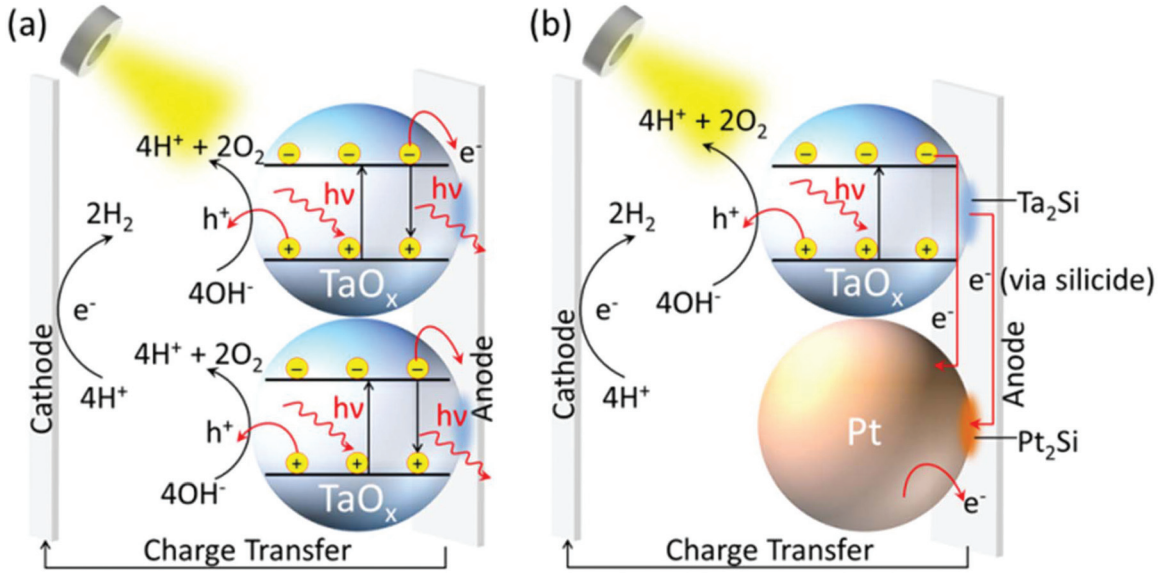

Fig. 5 Schematic diagrams of the mechanism of photoelectrochemical water splitting reactions for TaO_x NCs (a) without and (b) with Pt NCs co-deposited on H-Si. Due to the surface plasmonic effect of the Pt nanoclusters, most of the photogenerated electrons are concentrated at the metallic surface in close contact with the semiconductor TaO_x surface, which facilitates temporary charge holding upon charge separation.

Pt NCs) before recombination could occur, while the holes remain on the semiconducting TaO_x surface, thus promoting the production of H_2 and O_2. As illustrated in Fig. 2 and 3, the TaO_x NCs are uniformly distributed on the surface during soft landing. Given the separate locations of the Ta and Pt sputtering targets in the Nanogen source, the Pt NCs of nearly the same size as TaO_x NCs are found to deposit independently and uniformly on the H-Si substrate, filling the space between the TaO_x NCs, which leads to a well-mixed surface distribution of Pt and TaO_x NCs. With increasing proximity of Pt and TaO_x NCs with increasing deposition times, the charge transfer from the TaO_x to Pt NCs could proceed directly across the NC surfaces. In separate experiments, we have verified that Pt NCs alone exhibit almost no water splitting activity when tested under similar conditions. As discussed below, the observed enhanced photoconversion efficiency upon addition of Pt NCs to the semiconductor photocatalysts is therefore particularly remarkable. Furthermore, Pt_2Si found only at the interface of Pt NCs and the Si substrate is not illuminated directly by light and it therefore does not contribute to the water splitting activity. This is consistent with the fact that there is no report to date on the photoelectrochemical water splitting of Pt_2Si. The Pt NCs therefore serve, in effect, as the promoters to the TaO_x photocatalysts by providing "temporary" charge holding tanks to arrest the quick recombination process at the semiconductor surface.

Fig. 6a compares the photocurrent density profiles observed for six different (TaO_x, Pt) NC composite samples, four of which consist of a fixed amount of TaO_x NCs (obtained with 30 min deposition) and different amounts of co-deposited Pt NCs (Fig. 2). Evidently, increasing the relative amount of the Pt NC promoters from 0 to 15 to 30 min deposition has increased the photocurrent density from 0.24 to 0.33 to 0.46 mA cm^{-2} at 0.4 V *vs.* Ag/AgCl because more and more Pt NCs would be in closer proximity with TaO_x NCs with increasing Pt NC surface density. For Pt NC loading with 45 min deposition, however, the photocurrent density is found to decrease discernibly. This reduction could likely be due to overloading of the Pt NCs in the composite system, the excess of which physically block the photosensitive TaO_x surface, consequently reducing the surface concentrations of the electrons and holes produced by the reaction.

Since we have not observed alloy NC formation while co-depositing TaO_x and Pt NCs together, simultaneous co-deposition and sequential deposition are expected to produce similar results for the samples with sub-monolayer coverage. When the amount of material loading increases, the present co-deposition process becomes more effective in enhancing plasmonic activities because it creates a composite film with well mixed distributions of TaO_x and Pt NCs. Sequential deposition, however, could enable us to vary the size of the Pt NC promoters independently by employing different deposition parameters (after the deposition of TaO_x NCs). This method could therefore be used to incorporate a greater number of smaller Pt NCs into the system without blocking the photosensitive TaO_x surface and thus provide an even higher rate of electron–hole separation to enhance water splitting. By reducing the size of the Pt NCs from 5 to 3.5 and 2.5 nm, the photocurrent density is found to increase further in a near linear fashion with decreasing Pt NC size, from 0.46 mA cm^{-2} for 5 nm to 0.70 mA cm^{-2} for 3.5 nm to 1.1 mA cm^{-2} for 2.5 nm, all measured at 0.4 V *vs.* Ag/AgCl. In Fig. S1 (ESI†), we compare the photocurrent densities of the (TaO_x, Pt) NC composite with different Pt NC sizes obtained under chopped

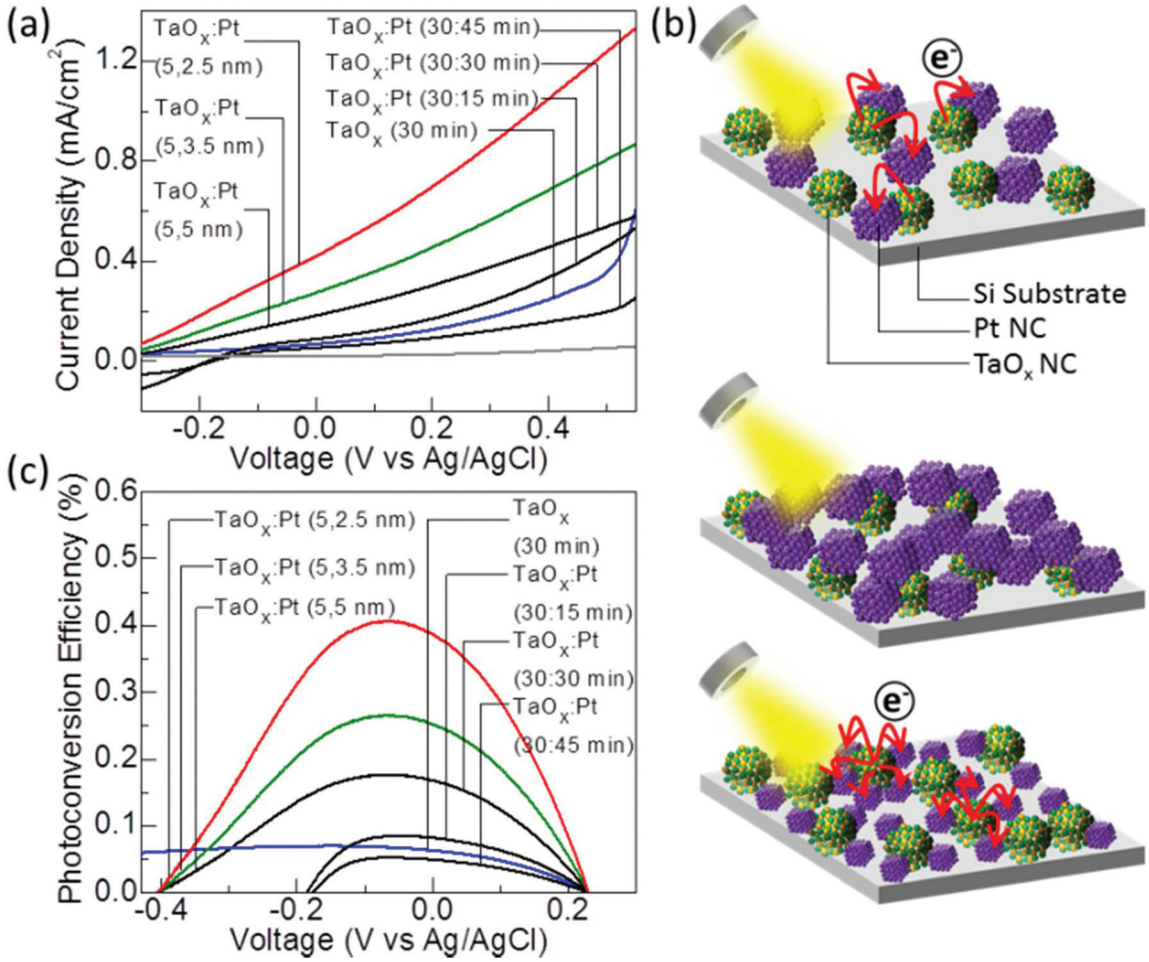

Fig. 6 (a) Photocurrent density and (c) photoconversion efficiency as functions of applied potential obtained for photoelectrochemical water splitting in a 1 M KOH electrolyte, using different composites of (TaO_x, Pt) nanoclusters (NCs) with different amounts and mode sizes supported on H-Si substrates as the photoanodes, all obtained with an illumination area of 5 × 5 mm^2 under a 300 W Xe lamp coupled with an AM 1.5 G filter at a power density of 50 mW cm^{-2}. (b) Schematic illustration of the advantage of using size-selected Pt NC promoters in the (TaO_x, Pt) NC composites for photocatalysis. TaO_x NCs are shown as spheres with Ta atoms in green and O atoms in yellow while the Pt NCs are represented by cubes of Pt atoms in purple. Arrows indicate the directions of the charge transfer (of electrons after electron–hole pair generation) from the semiconducting TaO_x NCs to the plasmonic Pt NCs serving as a temporary charge holding tank (top figure). For TaO_x and Pt NCs with the same size, overpopulation of Pt NCs could block the TaO_x surfaces (middle figure). By employing smaller Pt NCs to increase the lateral contact of the TaO_x NCs with a large number of smaller Pt NC neighbours, such surface blocking could be minimized and a greater photoconversion efficiency could be achieved (bottom figure).

AM 1.5 illumination during voltage sweep, which allows the dark and light currents to be monitored simultaneously confirming the photosensitive catalytic behavior. The stability of our photoanode system is also verified by measuring the photocurrent density during continuous light illumination over a 6-hour period, and it is found to exhibit only less than 1.5% decrease (Fig. S2, ESI†). Finally, the observed photocatalytic activity is achieved from nearly equal contribution from both UV and visible regions of the solar spectrum (Fig. S3, ESI†).

Fig. 6b schematically shows the proposed charge transfer mechanism from the semiconductor (TaO_x) surface to the metal (Pt) surface for different amounts and sizes of the plasmonic Pt NCs. In the case of the (TaO_x, Pt) NC composite with the same NC size (top), charge transfer is expected to increase with increasing Pt NCs surrounding the TaO_x NCs. When the amount of Pt NCs has become so large that excess Pt NCs begin to cover the TaO_x NCs, the water splitting activity will be reduced due to blocking of sunlight from reaching the surfaces of the TaO_x NCs (middle). On the other hand, reducing the size of Pt NCs will create more room for adding a larger number of smaller Pt NCs without surface blockage (bottom). As the TaO_x NCs will be surrounded by more Pt NCs, the charge transfer process would be greatly enhanced, producing a greater photoconversion efficiency.

In Fig. 6c, we summarize the photoconversion efficiency as a function of voltage for the aforementioned (TaO_x, Pt) NC composite photoanodes. The photoconversion efficiency of the water splitting reaction in the presence of external applied potential is given by the expression: $\frac{J_p(E^\circ_{rev} - E_{app})}{I_0}$, where J_p is

the observed photocurrent density; E°_{rev} is the standard reversible potential (*i.e.*, 1.23 V *vs.* RHE for the water splitting reaction); E_{app} is the applied potential *vs.* RHE; and I_0 is the power density of the incident light. By setting E_{app} to zero, the efficiency becomes the total photoconversion efficiency.[44,45] For the efficiency calculation, E_{app} *vs.* Ag/AgCl can be converted to E_{app} *vs.* RHE by using the Nernst equation ($E_{RHE} = E_{Ag/AgCl} + 0.059pH + E^{\circ}_{Ag/AgCl}$), where $E_{Ag/AgCl}$ is the applied potential *vs.* Ag/AgCl, pH for 1 M KOH is 13.2 and $E^{\circ}_{Ag/AgCl}$ is the standard Ag/AgCl electrode potential (*i.e.*, 0.197 V). Evidently, the photoconversion efficiency depends on the amount of material loading on the substrate because of the amount of active surface sites available for the reaction. The highest photoconversion efficiency of 0.41% is obtained for the (TaO_x, Pt: 5, 2.5 nm) NC composite with co-deposition for 30 min (Fig. 6a), which leads to the corresponding total photoconversion efficiency of 1.05%. This corresponds to the highest ever photoconversion efficiency observed for such a nanocluster system, and the NC composite photoanode is also among the top 10% of the best photoelectrochemical catalyst performers based on Ta_2O_5 nanostructures, with their photoconversion efficiencies reported in the range of 0.01–2.0%.[46,47] In marked contrast to all reported cases, all of which employ significantly larger amounts of materials and therefore provide potentially much larger numbers of active sites for the reaction,[29,47] the NC composite photoanode has only ~20% NC coverage on the substrate (as estimated using the ImageJ software). Extrapolating to a 100% coverage, the photoconversion efficiency of our (TaO_x, Pt) NC composite photoanode could potentially be increased fivefold to 5.25%. This efficiency will surpass the highest efficiency reported for chemically modified (metal doped or nitrogen doped) Ta_2O_5 nanostructures (such as nanotubes and nanorods) and thin films[46–48] as well as other Ta-based photocatalysts,[49,50] which will put our NC composite system to be among the best such photocatalysts with just a monolayer coverage. By depositing our size-selected NCs produced in a highly controllable environment onto different nanostructured substrates instead of the present planar substrate, the surface area of the substrate and, therefore, the amount of these size-selected nanoclusters could be further increased multifold, which could further enhance the efficiency. In addition, the high photoconversion efficiency achieved here is especially remarkable because the present tantalum oxide photocatalyst system is obtained without the need for any post-synthesis modification, in marked contrast to other reported catalysts, to which different chemical treatments have been applied to modify the morphology and/or structure of the active surfaces in order to enhance the water splitting reaction and to achieve better solar energy harvesting.[48,51]

Conclusion

We have successfully synthesized and deposited size-selected TaO_x and Pt NCs on H-Si substrates at room temperature under soft landing conditions using a magnetron-based nanocluster source equipped with a quadrupole mass filter. The as-grown NCs are found to be nearly monosized and uniformly distributed over the entire surface (without surface agglomeration), where defect-rich, amorphous TaO_x NCs (with a typical mode size of 5 nm) are well mixed with nanocrystalline Pt NCs (also with a mode size of 5 nm). Using a different amount of deposition time for each sputtering target, the amount of material loading can be effectively controlled and their effects are studied in a photoelectrochemical water splitting reaction. The most significant result of the present work is that by introducing Pt NC promoters to reduce the recombination rate of electron–hole pairs generated in the semiconductor TaO_x NC photocatalysts, the photoconversion efficiency can be greatly enhanced. The defect-rich TaO_x NC photocatalysts with a high specific surface area, along with the crystalline metallic Pt NC promoters, contribute to the observed enhanced photoelectrochemical performance. The total photoconversion efficiency is found to increase from 0.15% for the TaO_x NC photoanode without Pt NC promoters to 0.4% for the TaO_x NC photoanode with Pt NC promoters (both of 5 nm in size). The highest photocatalytic activity for the water splitting reaction is observed when the amount of Pt NCs is increased to almost the same as that of the TaO_x NCs, while a higher Pt NC loading leads to blockage of photoelectrochemically active surface of TaO_x, thereby reducing the observed photocatalytic activity. The surface blocking issue is resolved by reducing the Pt NC size (from 5 nm to 2.5 nm) and the efficiency is found to increase by 2.5 times to 1.05% with only 20% surface coverage. Along with the concept of reaction promoters in a nanocomposite system, the use of size-selected, ultrasmall metal/metal oxide nanoclusters below 10 nm (as produced by the novel Nanogen nanocluster source coupled with a quadrupole mass filter) can be extended to other applications in catalysis, chemical sensing, and nanoelectronics.

Acknowledgements

This work was supported by the Natural Sciences and Engineering Research Council of Canada.

References

1 E. Roduner, *Chem. Soc. Rev.*, 2006, **35**, 583–592.
2 G. Schmid, *Adv. Eng. Mater.*, 2001, **3**, 737–743.
3 L. S. Ott and R. G. Finke, *Coord. Chem. Rev.*, 2007, **251**, 1075–1100.
4 J. Li, S. Guo and E. Wang, *RSC Adv.*, 2012, **2**, 3579–3586.
5 G. Schmid, M. Bäumle, M. Geerkens, I. Heim, C. Osemann and T. Sawitowski, *Chem. Soc. Rev.*, 1999, **28**, 179–185.
6 U. Heiz and E. L. Bullock, *J. Mater. Chem.*, 2004, **14**, 564–577.
7 J. Wang, B. Sun, F. Gao and N. C. Greenham, *Phys. Status Solidi*, 2010, **207**, 484–487.

8 N. Han, F. Wang, J. J. Hou, S. P. Yip, H. Lin, F. Xiu, M. Fang, Z. Yang, X. Shi, G. Dong, T. F. Hung and J. C. Ho, *Adv. Mater.*, 2013, **25**, 4445–4451.

9 M. Chen, T. P. Straatsma and D. A. Dixon, *J. Phys. Chem. A*, 2015, **119**, 11406–11421.

10 E. Sattler, K. Muhlbach and J. Recknagel, *Phys. Rev. Lett.*, 1980, **45**, 821–824.

11 R. E. Dietz, T. G. Duncan, M. A. Powers and D. E. Smalley, *J. Chem. Phys.*, 1981, **74**, 6511–6512.

12 M. A. Gracia-Pinilla, E. Perez-Tijerina, J. A. Garcia, A. Tlahuice-Flores, S. Mejia-Rosale, J. M. Montejano-Carrizales and M. Jose-Yacaman, *J. Phys. Chem. C*, 2008, **112**, 13492–13498.

13 M. Drabik, A. Choukourov, A. Artemenko, O. Polonskyi, O. Kylian, J. Kousal, L. Nichtova, V. Cimrova, D. Slavinska and H. Biederman, *J. Phys. Chem. C*, 2011, **115**, 20937–20944.

14 R. E. Palmer, S. Pratontep and H. G. Boyen, *Nat. Mater.*, 2003, **2**, 443–448.

15 S. Srivastava, J. P. Thomas, A. Rahman, M. Abd-ellah, M. Mohapatra, D. Pradhan, N. F. Heinig and K. T. Leung, *ACS Nano*, 2014, **8**, 11891–11898.

16 S. In, A. H. Kean, A. Orlov, M. S. Tikhov and R. M. Lambert, *Energy Environ. Sci.*, 2009, **2**, 1277–1279.

17 T. Momin and A. Bhowmick, *Rev. Sci. Instrum.*, 2010, **81**, 075110.

18 M. Gracia-Pinilla, E. Martínez, G. S. Vidaurri and E. Pérez-Tijerina, *Nanoscale Res. Lett.*, 2009, **5**, 180–188.

19 K. Bromann, C. Felix, H. Brune, W. Harbich, R. Monot, J. Buttet and K. Kern, *Science*, 1996, **274**, 956–958.

20 S. M. Lang and T. M. Bernhardt, *Phys. Chem. Chem. Phys.*, 2012, **14**, 9255–9269.

21 A. I. Ayesh, N. Qamhieh, H. Ghamlouche, S. Thaker and M. El-Shaer, *J. Appl. Phys.*, 2010, **107**, 034317.

22 E. Pérez-Tijerina, M. Gracia Pinilla, S. Mejía-Rosales, U. Ortiz-Méndez, A. Torres and M. José-Yacamán, *Faraday Discuss.*, 2008, **138**, 353–362.

23 F. Yin, Z. W. Wang and R. E. Palmer, *J. Exp. Nanosci.*, 2012, **7**, 703–710.

24 I. Shyjumon, M. Gopinadhan, C. A. Helm, B. M. Smirnov and R. Hippler, *Thin Solid Films*, 2006, **500**, 41–51.

25 M. Wajid Shah, Y. Zhu, X. Fan, J. Zhao, Y. Li, S. Asim and C. Wang, *Sci. Rep.*, 2015, **5**, 1–8.

26 X. Zhang, H. Yang, B. Zhang, Y. Shen and M. Wang, *Adv. Mater. Interfaces*, 2016, **3**, 1500273.

27 P. Thangadurai, I. Zergioti, S. Saranu, C. Chandrinou, Z. Yang, D. Tsoukalas, A. Kean and N. Boukos, *Appl. Surf. Sci.*, 2011, **257**, 5366–5369.

28 H. Kim, D. Monllor-Satoca, W. Kim and W. Choi, *Energy Environ. Sci.*, 2015, **8**, 247–257.

29 P. Zhang, J. Zhang and J. Gong, *Chem. Soc. Rev.*, 2014, **43**, 4395–4422.

30 Y. Takahara, J. N. Kondo, T. Takata, D. Lu and K. Domen, *Chem. Mater.*, 2001, **13**, 1194–1199.

31 W. Chun, A. Ishikawa, H. Fujisawa, T. Takata, J. N. Kondo, M. Hara, M. Kawai, Y. Matsumoto and K. Domen, *J. Phys. Chem. B*, 2003, **107**, 1798–1803.

32 Y. Noda, B. Lee, K. Domen and J. N. Kondo, *Chem. Mater.*, 2008, **20**, 5361–5367.

33 G. P. Zhmurko, V. N. Kuznetsov, K. B. Kalmykov and T. G. Murzagareev, *J. Alloys Compd.*, 1996, **240**, 249–252.

34 J. M. Gregoire, M. E. Tague, S. Cahen, S. Khan, H. D. Abruña, F. J. DiSalvo and R. B. van Dover, *Chem. Mater.*, 2010, **22**, 1080–1087.

35 H. Haberland, M. Karrais and M. Mall, *Z. Phys. D: At., Mol. Clusters*, 1991, **20**, 413–415.

36 Y. Haberland, H. Mall, M. Moseler, M. Qiang, Y. Reiners and T. Thurner, *J. Vac. Sci. Technol., A*, 1994, **12**, 2925–2930.

37 S. Srivastava, PhD Thesis, University of Waterloo, 2016.

38 X. Liu, E. Koposova, A. Offenhäusser and Y. Mourzina, *RSC Adv.*, 2015, **5**, 86934–86940.

39 S. Hashimoto, C. Tanaka, A. Murata and T. Sakurada, *J. Surf. Anal.*, 2006, **13**, 14–18.

40 M. Zier, S. Oswald, R. Reiche and K. Wetzig, *Anal. Bioanal. Chem.*, 2003, **375**, 902–905.

41 F. de Root and A. Kotani, in *Core Level Spectroscopy of Solids*, CRC Press, 2008, pp. 230–232.

42 Z. Zhang, L. Zhang, M. N. Hedhili, H. Zhang and P. Wang, *Nano Lett.*, 2013, **13**, 14–20.

43 J. Lee, S. Mubeen, X. Ji, G. D. Stucky and M. Moskovits, *Nano Lett.*, 2012, **12**, 5014–5019.

44 M. A. Rahman, S. Bazargan, S. Srivastava, X. Wang, M. Abd-Ellah, J. P. Thomas, N. F. Heinig, D. Pradhan and K. T. Leung, *Energy Environ. Sci.*, 2015, **8**, 3363–3373.

45 S. U. M. Khan, M. Al-Shahry and W. B. Ingler, *Science*, 2002, **297**, 2243–2245.

46 Y. Li, K. Nagato, J. J. Delaunay, J. Kubota and K. Domen, *Nanotechnology*, 2014, **25**, 014013.

47 A. Dabirian, H. V. Spijker and R. Van De Krol, *Energy Procedia*, 2011, **22**, 15–22.

48 L. Wang, X. Zhou, N. T. Nguyen, I. Hwang and P. Schmuki, *Adv. Mater.*, 2016, **28**, 2432–2438.

49 G. Wang, H. Wang, Y. Ling, Y. Tang, X. Yang, R. C. Fitzmorris, C. Wang, J. Z. Zhang and Y. Li, *Nano Lett.*, 2011, **11**, 3026–3033.

50 N. Roy, Y. Sohn and D. Pradhan, *ACS Nano*, 2013, **7**, 2532–2540.

51 N. K. Allam, B. S. Shaheen and A. M. Hafez, *ACS Appl. Mater. Interfaces*, 2014, **6**, 4609–4615.